Chapter 4

Control field

In this chapter, the implementation of an active noise control model to the ducted fan noise prediction code TBIEM3D is described. Section 4.1 describes the analytical modeling of the control field, and section 4.2 describes the active noise control algorithms that were used in this study to adjust the control field (i.e., the outputs from the control sources) such that reduction of the radiated fan noise is achieved.

4.1 Analytical model

The implementation of active noise control to the TBIEM3D code has to be done in a manner that is compatible with the BIEM method. The active noise control implementation should not introduce any assumptions that would compromise the effectiveness and capabilities of the duct fan noise prediction code TBIEM3D. Thus, if infinite duct theory were to be used to model the modes that are generated by the control sources and that propagate in the duct, TBIEM3D would be constrained to consider only ducts of a simple cylindrical shape, and reflection at the duct openings of the modes generated by the control sources would be neglected. Also, use of the Rayleigh integral (as in almost all of the models reviewed in section 1.3) to compute the radiation of the control modes into the far field would imply that the duct is embedded in a baffle and

would therefore limit the computation of the controlled pressure field to the region upstream or downstream of the duct opening. This approach would prevent the user from taking advantage of TBIEM3D ‘s ability to compute noise radiation in the shadow region (i.e., to the side) of the duct.

By computing the field generated by the control sources in the same manner as the fan noise field was computed, the control field would implicitly include reflection from the duct openings, upstream and downstream radiation, refraction at the edges of the duct, etc.. With this approach, the features that would make an active noise control model more advanced than current ones would be preserved. Hence, a scattering approach is used to compute the control field. The field generated by the control sources in free space is computed first, and is then used to compute the scattered component of the control field through the BIEM procedure described in Chapter 2. The analytical expression for the incident field generated by the control sources is derived next.

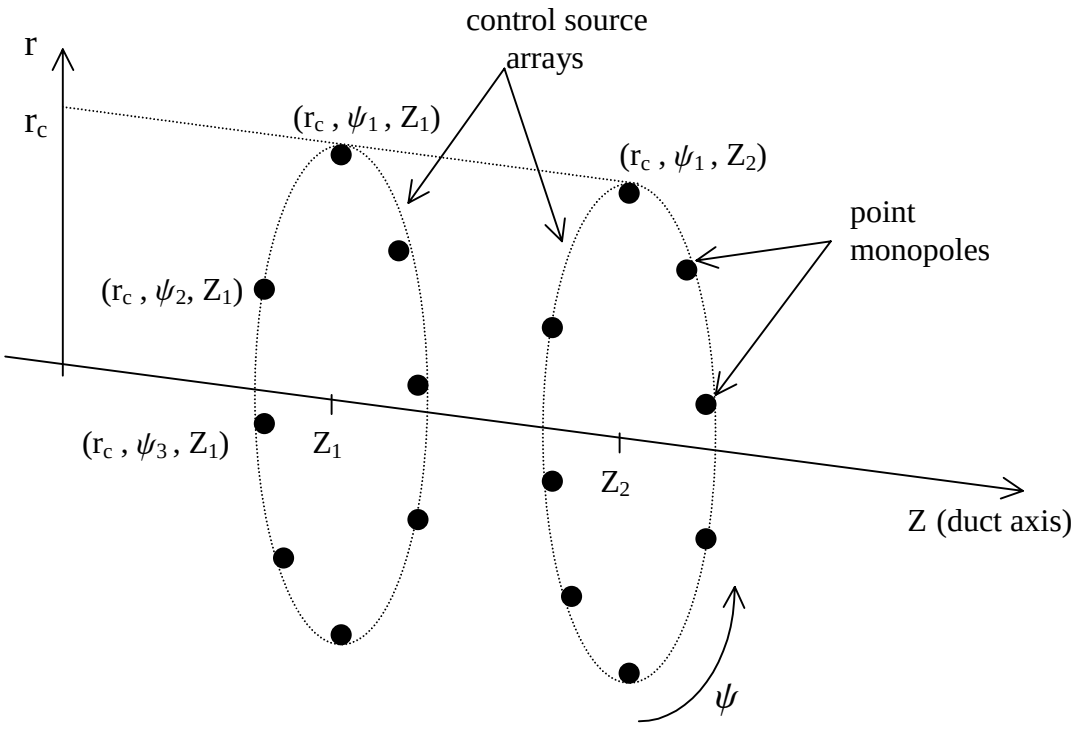

Figure 4.1: Control source model

The control sources are modeled by point monopoles and are organized into N_a axial arrays of N_c point monopoles placed along the duct inlet inner wall at $r=r_c$ where $r_c \le r_d$; $z=z_l$, $l=1,2,...,N_a$; $\psi=\psi_j$, $j=1,2,...N_c$, as described in Figure 4.1.

The incident field generated by the control sources is obtained by solving the following wave equation in an unbounded space

$$[\frac{1}{\tilde{c}^2}\frac{\partial^2}{\partial\tilde{t}^2}-\frac{1}{\tilde{r}}\frac{\partial}{\partial\tilde{r}}(\tilde{r}\frac{\partial}{\partial\tilde{r}})-\frac{1}{\tilde{r}^2}\frac{\partial^2}{\partial\psi^2}-\frac{\partial^2}{\partial\tilde{z}^2}]\tilde{p}_i(\tilde{r},\psi,\tilde{z},\tilde{t})=$$

$$\sum_{l=1}^{N_a}\sum_{j=1}^{N_c}\tilde{q}_{j,l}\frac{\delta(\tilde{r}-\tilde{r}_c)}{\tilde{r}}\,\delta(\tilde{z}-\tilde{z}_l-\tilde{V}\tilde{t})\;\delta(\psi-\psi_j)e^{i\tilde{\omega}\tilde{t}} \qquad (4.1)$$

where $q_{j,l}$ is the strength of the j^{th} source in the l^{th} array and ω is the frequency of excitation of the control sources. Reflections from the fan are not taken into account.

The procedure used in Chapter 3 to find the solution of the inhomogeneous wave equation describing the fan noise radiation is also used in this section to compute the solution of Eq. (4.1).

First, Eq. (4.1) is nondimensionalized, yielding

$$[\frac{1}{c^2}\frac{\partial^2}{\partial t^2}-\frac{1}{r}\frac{\partial}{\partial r}(r\frac{\partial}{\partial r})-\frac{1}{r^2}\frac{\partial^2}{\partial\psi^2}-\frac{\partial^2}{\partial z^2}]\,p_i(r,\psi,z,t)=$$

$$\sum_{l=1}^{N_a}\sum_{j=1}^{N_c}q_{j,l}\frac{\delta(r-r_c)}{r}\,\delta(z-z_l-Vt)\;\delta(\psi-\psi_j)e^{i\omega t}. \qquad (4.2)$$

Next, this equation is expressed in the stretched, moving frame of coordinates described previously by Eq. (3.17) and Eq. (3.18). In that reference frame, Eq. (4.2) is written as

$$[\frac{1}{c^2}\left(\frac{\partial}{\partial t}-\frac{V}{\beta}\frac{\partial}{\partial Z}\right)^2-\frac{1}{r}\frac{\partial}{\partial r}(r\frac{\partial}{\partial r})-\frac{1}{r^2}\frac{\partial^2}{\partial\psi^2}-\frac{1}{\beta^2}\frac{\partial^2}{\partial Z^2}]p_i(r,\psi,Z,t)=$$

$$\sum_{l=1}^{N_a}\sum_{j=1}^{N_c}q_{j,l}\,\frac{\delta(r-r_c)}{r}\,\frac{\delta(Z-Z_l)}{\beta}\,\delta(\psi-\psi_j)\,e^{i\omega t} \qquad (4.3)$$

Now, it is noted that the term $\sum_{l=1}^{N_a}\sum_{j=1}^{N_c} q_{j,l}\,\delta(\psi-\psi_j)$ is a periodic function, of period 2π, that can be expanded into a Fourier series and rewritten as

$$\sum_{l=1}^{N_a}\sum_{j=1}^{N_c} q_{j,l}\,\delta(\psi-\psi_j)=\sum_{m=-\infty}^{\infty} c_m\, e^{-im\psi}, \tag{4.4}$$

where

$$c_m=\frac{1}{2\pi}\sum_{l=1}^{N_a}\sum_{j=1}^{N_c} q_{j,l}\int_0^{2\pi}\delta(\psi-\psi_j)\, e^{im\psi}\,d\psi, \tag{4.5}$$

or,

$$c_m=\frac{1}{2\pi}\sum_{l=1}^{N_a}\sum_{j=1}^{N_c} q_{j,l}\; e^{im\psi_j}\;. \tag{4.6}$$

Therefore, Eq. (4.3) becomes

$$\left[\frac{1}{c^2}\left(\frac{\partial}{\partial t}-\frac{V}{\beta}\frac{\partial}{\partial Z}\right)^2-\frac{1}{r}\frac{\partial}{\partial r}\left(r\frac{\partial}{\partial r}\right)-\frac{1}{r^2}\frac{\partial^2}{\partial\psi^2}-\frac{1}{\beta^2}\frac{\partial^2}{\partial Z^2}\right]p_i(r,\psi,Z,t)=$$
$$\frac{1}{2\pi}\frac{\delta(r-r_c)}{r}\sum_{m=-\infty}^{\infty}\sum_{l=1}^{N_a}\sum_{j=1}^{N_c} q_{j,l}\,\frac{\delta(Z-Z_l)}{\beta}\, e^{-im(\psi-\psi_j)}\; e^{i\omega t} \tag{4.7}$$

Assuming that the solution of the above equation is of the form

$$p_i(r,\psi,z,t)=\sum_{m=-\infty}^{\infty} P_i^m(r,Z)\, e^{-im\psi}\; e^{i\omega t}, \tag{4.8}$$

Eq. (4.7) can be written as

$$\left[\frac{1}{c^2}\left(i\omega-\frac{V}{\beta}\frac{\partial}{\partial Z}\right)^2-\frac{1}{r}\frac{\partial}{\partial r}\left(r\frac{\partial}{\partial r}\right)+\frac{m}{r^2}-\frac{1}{\beta^2}\frac{\partial^2}{\partial Z^2}\right]P_i^m(r,Z)$$
$$\frac{1}{2\pi}\frac{\delta(r-r_c)}{r}\sum_{l=1}^{N_a}\sum_{j=1}^{N_c} q_{j,l}\,\frac{\delta(Z-Z_l)}{\beta}\, e^{im\psi_j}\;. \tag{4.9}$$

Let

$$\tilde{\omega}=n_h N\tilde{\Omega}, \tag{4.10}$$

where $n_h N\tilde{\Omega}$ was defined in Chapters 2 and 3 as the fan blade passage frequency and its associated harmonics. In a feedforward control algorithm these frequencies will correspond to the frequencies of excitation $\tilde{\omega}$ of the control sources.

Also, let

$$m = n_h N \tag{4.11}$$

where $n_h N$ is the circumferential order of the modes generated by the fan and m is the circumferential order of the modes generated by the control sources. From Eq. (4.10), Eq. (4.11) and Eq. (3.28),

$$\frac{\omega}{c} = \frac{\omega}{\tilde{\Omega}}\frac{\tilde{\Omega}\tilde{r}_d}{\tilde{c}} = \frac{\tilde{\omega}}{\tilde{c}}\tilde{r}_d = \frac{n_h N\tilde{\Omega}}{\tilde{c}}\tilde{r}_d = \frac{n_h N}{c} = \frac{m}{c}. \tag{4.12}$$

Thus, combining Eq. (4.12) with Eq. (4.9) yield

$$\left[\frac{1}{c^2}\left(im - \frac{V}{\beta}\frac{\partial}{\partial Z}\right)^2 - \frac{1}{r}\frac{\partial}{\partial r}\left(r\frac{\partial}{\partial r}\right) + \frac{m}{r^2} - \frac{1}{\beta^2}\frac{\partial^2}{\partial Z^2}\right]P_i^m(r,Z)$$

$$\frac{1}{2\pi}\frac{\delta(r-r_c)}{r}\sum_{l=1}^{N_a}\sum_{j=1}^{N_c} q_{j,l}\frac{\delta(Z-Z_l)}{\beta}e^{im\psi_j}. \tag{4.13}$$

It is observed that the left hand side of this equation is of the same form as the left hand side of Eq. (3.26). Therefore, referring to the analysis done in section 3.2.1 (Eq. (3.28) through Eq. (3.33)), Eq. (4.13) can be written as

$$\left[\frac{\partial^2}{\partial Z} + \kappa^2 + \frac{1}{r}\frac{\partial}{\partial r}\left(r\frac{\partial}{\partial r}\right) - \frac{m^2}{r^2}\right]e^{i\kappa M Z}\,P_i^m(r,Z) =$$

$$\frac{-1}{2\pi}e^{i\kappa M Z}\frac{\delta(r-r_c)}{r}\sum_{l=1}^{N_a}\sum_{j=1}^{N_c} q_{j,l}\frac{\delta(Z-Z_l)}{\beta}e^{im\psi_j}, \tag{4.14}$$

where κ is defined by Eq. (3.27). Introducing the following variable

$$Q_i^m(r,Z) = e^{i\kappa M Z}\,P_i^m(r,Z), \tag{4.15}$$

Eq. (4.14) becomes

$$\left[\frac{\partial^2}{\partial Z}+\kappa^2+\frac{1}{r}\frac{\partial}{\partial r}\left(r\frac{\partial}{\partial r}\right)-\frac{m^2}{r^2}\right]Q_i^m(r,Z)=$$

$$-\frac{1}{2\pi}\sum_{l=1}^{N_a}\sum_{j=1}^{N_c}q_{j,l}\,\frac{\delta(r-r_c)}{r}\,\frac{\delta(Z-Z_l)}{\beta}\,e^{i\kappa MZ}\,e^{im\psi_j}\quad . \tag{4.16}$$

This equation is the inhomogeneous Helmholtz equation for $Q_i(r,Z)$. The Green's function for the Helmholtz operator of this equation is known and is defined as

$$G_m(r,r',Z-Z')=\frac{1}{2\pi}\int_0^{\pi}\cos(m\psi')\,\frac{e^{-i\kappa R}}{R}\,d\psi' \tag{4.17}$$

where $R=\sqrt{r^2+r'^2-2rr'\cos\psi'+(Z-Z')^2}$ is the distance, in cylindrical coordinates, between two points M and M'.

Therefore, applying the Green's function technique, the solution of the Helmholtz equation is given by

$$Q_i^m(r,Z)=-\frac{1}{2\pi\beta}\sum_{l=1}^{N_a}\sum_{j=1}^{N_c}q_{j,l}\,e^{im\psi_j}$$

$$\int_{r'=0}^{\infty}\int_{Z'=-\infty}^{\infty}G_m(r,r',Z-Z')\,\delta(r'-r_c)\,\delta(Z'-Z_l)\,e^{i\kappa MZ'}\,dZ'\,dr'. \tag{4.18}$$

Noting that

$$\int_{r'=0}^{\infty}f(r')\,\delta(r'-r_0)\,dr'=f(r_0), \tag{4.19}$$

and

$$\int_{Z'=-\infty}^{\infty}f(Z')\,\delta(Z'-Z_0)\,dZ'=f(Z_0) \tag{4.20}$$

the solution of the inhomogeneous Helmholtz equation becomes

$$Q_i^m(r,Z)=-\frac{1}{2\pi\beta}\sum_{l=1}^{N_a}\sum_{j=1}^{N_c}q_{j,l}\,e^{im\psi_j}\,G_m(r,r_c,Z-Z_l)\,e^{i\kappa MZ_l}\quad , \tag{4.21}$$

i.e.,

$$Q_i^m(r,Z)=-\frac{1}{4\pi^2\beta}\sum_{l=1}^{N_a}\sum_{j=1}^{N_c}q_{j,l}\,e^{im\psi_j}\,e^{i\kappa MZ_l}\int_0^{\pi}\cos(m\psi')\,\frac{e^{-i\kappa R}}{R}\,d\psi'\ , \tag{4.22}$$

where

$$R = \sqrt{r^2 + r_c^{\,2} - 2\,r\,r_c \cos\psi' + (Z - Z_l)^2} \tag{4.23}$$

Therefore, the resulting expression for the pressure field generated in the unbounded space by the circumferential arrays of control sources (i.e., point monopoles) is

$$p_i(r,\psi,Z,t) = -\frac{1}{4\pi^2\beta} \sum_{m=-\infty}^{\infty} \sum_{l=1}^{N_a} \sum_{j=1}^{N_c} q_{j,l}\, e^{i m \psi_j}\, e^{i \kappa M (Z_l - Z)} \int_0^{\pi} \cos(m\psi') \frac{e^{-i\kappa R}}{R} d\psi'\; e^{-i m \psi}\, e^{i\omega t} \tag{4.24}$$

In order to compute the scattered field through the procedure described in Chapter 2, both the Q_i term defined by Eq. (4.23) and its derivative with respect to r need to be known. Taking the derivative of Eq. (4.23) with respect to r yields

$$\frac{\partial Q_i^m}{\partial r}(r,Z) = -\frac{1}{4\pi^2\beta} \sum_{l=1}^{N_a} \sum_{j=1}^{N_c} q_{j,l}\, e^{i m \psi_j}\, e^{i \kappa M Z_l} \int_0^{\pi} \cos(m\psi') (1 + i\kappa r)(r_c \cos\psi' - 1) \frac{e^{-i\kappa R}}{R^3} d\psi' \tag{4.25}$$

The terms described in Eq. (4.23) and Eq. (4.25) are computed numerically using the method of Gauss-Legendre for the integration procedure.

4.2 Active control algorithms

Feedforward active control systems were modeled in this study. Figure 4.2 shows a schematic of a feedforward active control system implemented in a turbofan engine inlet. The control sources are placed along the circumference of the duct inner wall while the error (pressure) sensors are positioned in the acoustic far field (shown) or along the duct

inner wall (not shown). The fan produces a disturbance sound field at the blade passage frequency and its harmonics. This unwanted noise field propagates through the duct and radiates into the far field. A sensor mounted on the engine, near the fan station, generates sinusoidal signals that are correlated with the blade passage frequency and harmonics and are input into an array of compensators. The outputs from the compensators are the control signals. The control sources (speakers), driven by the control signals, generates the secondary sound field that destructively interferes with the fan noise field.

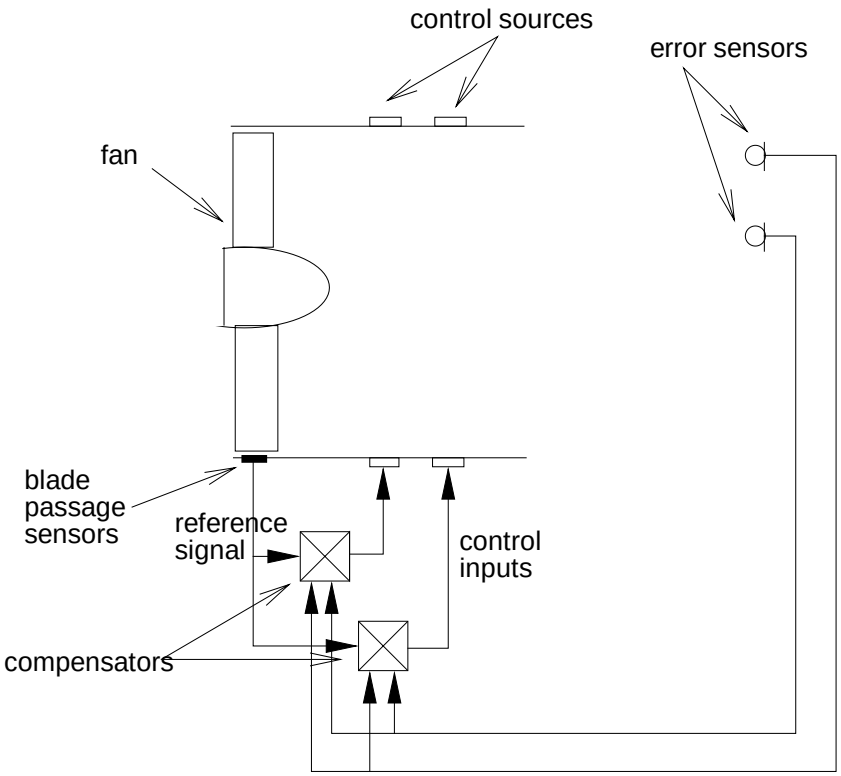

Figure 4.2: Schematic of a feedforward active control system.

In the control system configurations that were modeled in this work, the error sensors were microphones placed in the far field of the duct inlet and/or outlet, along the aircraft fuselage, or along the duct inner wall. The control algorithms corresponding to each modeled active control system configuration are described next.

4.2.1 Far field error sensors

A schematic of the control system configuration using error sensors placed in the far field of the inlet is presented in Figure 4.3.

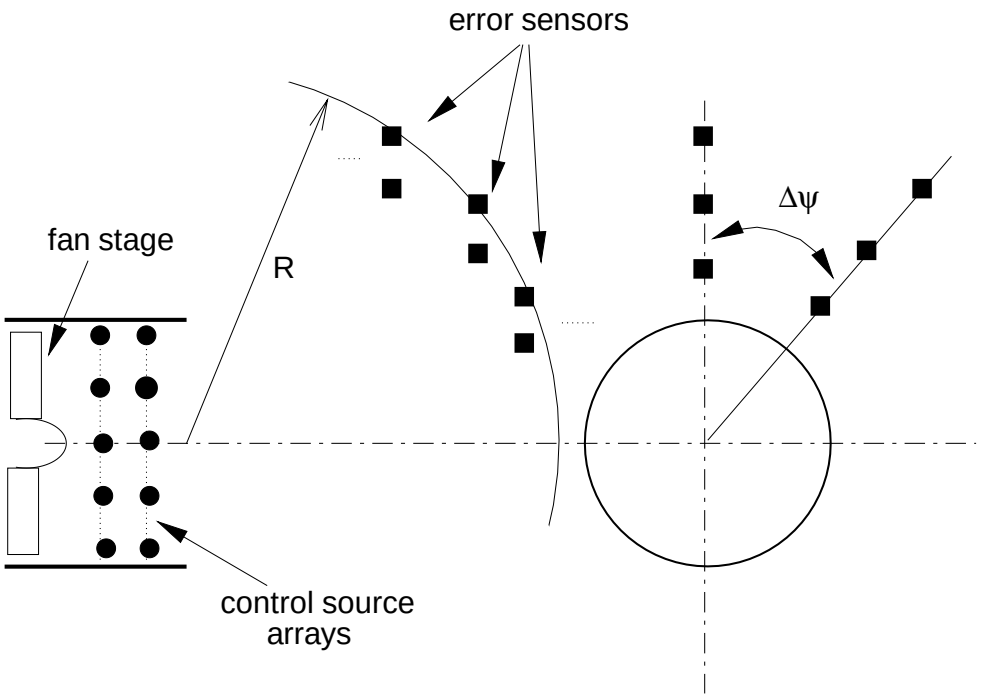

Figure 4.3: Schematic of a control system using far field error sensors.

A total of S control sources are placed along the duct inner wall (referring to section 4.1, $S=N_a*N_c$), and E error sensors are placed in the far field to monitor the radiated pressure. The control sources generate the secondary or control field aimed to destructively interfere with the primary field, i.e. the radiated fan noise. The control signals driving the control sources are determined so as to minimize the pressure at the error sensors location.

The pressure p_e^t at the e^{th} far field error sensor is the sum of the pressure p_e^p due to the primary field and the pressure p_e^s due to the secondary field at that error sensor, i.e.,

$$p_e^t = p_e^p + p_e^s \tag{4.26}$$

The control sources are grouped into control channels; the control sources within any given control channel are driven by the same control signal amplitude. Therefore, assuming that there is a total of L control channels, the pressure p_e^s due to all the control sources at the e^{th} error sensor is given by

$$p_e^s = (U)^T [R] (p_{e,s}), \; s=1,2,...,S \tag{4.27}$$

where [R] is the control source configuration matrix for the L control channels. [R] is of dimensions L×S. The elements $R_{l,s}$ of the matrix [R] are complex numbers that represent the magnitude and phase of each control source grouped into the l^{th} channel and driven by the l^{th} control amplitude U_l. For example, the following elements of the configuration matrix: 1, -1, i, -i and 0, where i corresponds to the complex number (0,1), represent in-phase, out-of-phase, 90 degrees out-of-phase, -90 degrees out-of-phase and disconnected condition, respectively. The elements of the vector $(U)^T$

$$(U)^T = (U_1, U_2, ..., U_L), \tag{4.28}$$

where the superscript ^{T} indicates transpose, are the control amplitudes driving each control channel. The elements of the vector $(p_{e,s})^T$

$$(p_{e,s})^T = (p_{e,1}, p_{e,2}, ..., p_{e,S}) \tag{4.29}$$

correspond to the pressure at the e^{th} error sensor due to each control source.

Thus, the total pressure at each far field error sensor can be expressed as

$$(p_e)^t_{e=1,2,...,E} = (p_e)^p_{e=1,2,...,E} + (U)^T [R] [p_{e,s}]_{e=1,2,...,E;\ s=1,2,...,S} \quad (4.30)$$

or

$$(p_e)^t_{e=1,2,...,E} = (p_e)^p_{e=1,2,...,E} + (U)^T [H]^T \quad (4.31)$$

where [H] is called the transfer matrix. [H] is of dimension E×L and its elements correspond to the complex output at each error sensors due to a unit input from each control channel.

The optimum complex control amplitude inputs, U_l, are obtained by minimizing a cost function, which is defined as the sum of the squared moduli of the pressures at the error sensors, i.e,

$$J = (p_e)^{t\,H} (p_e)^t \quad (4.32)$$

where the superscript ^{H} denotes the complex conjugate of the vector transpose.

It can be shown that J is a quadratic function of the complex control amplitudes U_l (Nelson and Elliott 1992), which has a global minimum for a certain control amplitude vector (U). This optimum vector (U) can be evaluated by setting to zero the derivatives of J with respect to the real and imaginary part of the control amplitudes. The optimum control amplitude vector is then given by

$$(U)_{opt} = - ([H]^H [H])^{-1} [H]^H (p_e)^p_{e=1,2,...,E} \quad (4.33)$$

For the case of equal number of error sensors and control channels (i.e. E=L), the above equation reduces to

$$(U)_{opt} = - ([H])^{-1} (p_e)^p_{e=1,2,...,E} \quad (4.34)$$

and the pressure at all the error sensors is theoretically driven to zero.

4.2.2 Fuselage error sensors

A schematic of the configuration of the control system using fuselage error sensors is presented in Figure 4.4.

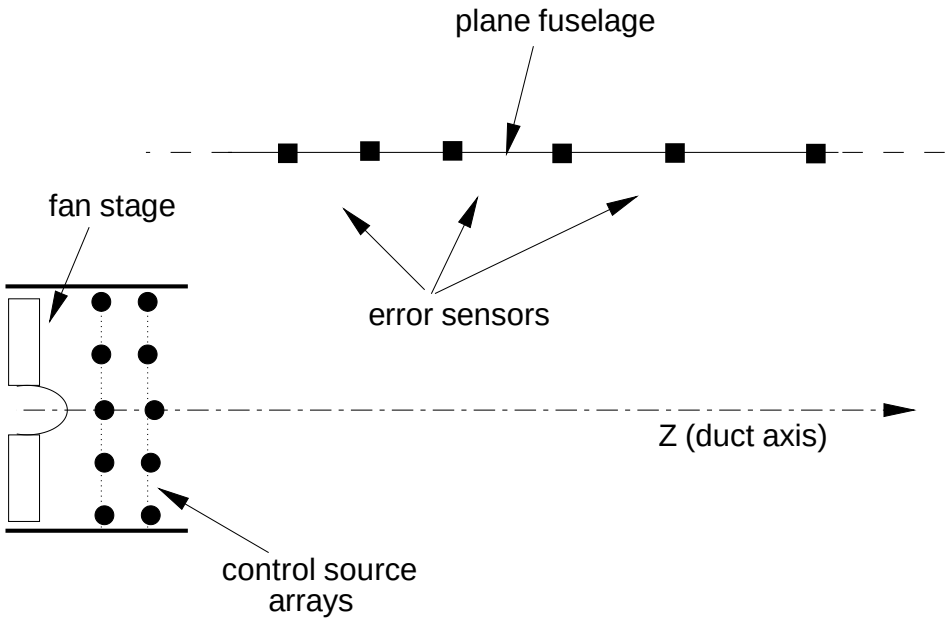

Figure 4.4: Schematic of a control system using fuselage error sensors.

The error sensors are placed along the fuselage of the aircraft in a configuration that is parallel to the axis of the fan duct. Since the error sensors are all located within a single plane (r,ψ_0, Z), they will not be able to register the necessary phase information that will indicate to the controller that spinning modes need to be targeted for control. This

inability would prevent the controller from driving the control sources to generate spinning modes. To overcome this problem, the control system is pre-configured in a manner that will ensure the generation of spinning modes that will destructively interfere with the ones generated by the fan: in order to generate the m^{th} order circumferential spinning mode, each control source array is composed of 4m control sources (Burdisso et al. 1995) and is driven by a single control channel. In each control array, the control sources are evenly distributed around the circumference of the duct and the phase shift between successive control sources is set to 90 degrees. So, in the case were a single control source array is used to generate the control field, the configuration matrix R (cf. section 4.2.1) reduces to a line vector formed by the sequence (1, i, -1, -i) repeated four times, and Eq. (4.30) becomes

$$(p_e)^t_{e=1,2,\ldots,E} = (p_e)^p_{e=1,2,\ldots,E} + U_1\,(1, i, -1, -i, 1, i, -1, -i, \ldots)\,[p_{e,s}]_{e=1,2,\ldots,E;\ s=1,2,\ldots,16.} \qquad (4.35)$$

Since the duct modes are assumed to radiate axisymmetrically from the duct openings, this configuration of the control system is also expected to minimize the noise radiating toward the ground: by reducing the sound radiation toward the fuselage within a certain sector, one will also implicitly reduce the sound radiation toward the ground within that same sector. In the instance where the modes radiating from the duct openings can not be assumed to be axisymmetrical, additional axial arrays of error sensors could be placed around the aircraft fuselage in order to control the sound radiation at different azymuthal angles.

4.2.3 Wavenumber error sensors

With the wavenumber error sensors technique, instead of minimizing the pressure at the error sensors placed in the far field or along the aircraft fuselage, certain components of the axial wavenumber spectrum of the inlet (or outlet) duct sound field are minimized

in an attempt to reduce the acoustic radiation toward specific directions of the far field. The principle of this active noise control approach is described next. Wavenumber sensors were first implemented by (Smith and Burdisso 1999). Related details of the method can also be found in (Joseph et al. 1997).

The wave equation in a cylindrical duct with steady axial flow can be expressed as

$$\left(\frac{1}{c}\frac{\partial}{\partial t}+M\frac{\partial}{\partial z}\right)^2 p - \nabla^2 p = 0, \tag{4.36}$$

where M, the flow Mach number, is assumed negative in the inlet of the duct and positive in the outlet. Referring to section 3.1, the solution to Eq. (4.36) is of the form

$$p_{mn}(r,\psi,z) = A_{mn}\, J_m(k_{r\psi}^{mn} r)\, \exp(i[m(\Omega t-\psi)-k_z^{mn} z]). \tag{4.37}$$

Introducing Eq. (4.37) back into the convected wave equation, Eq. (4.36), leads to the following relation (Rice and Heidmann 1979)

$$k_{r\psi}^{mn\,2} + k_z^{mn\,2} = \left(k - M\, k_z^{mn}\right)^2. \tag{4.38}$$

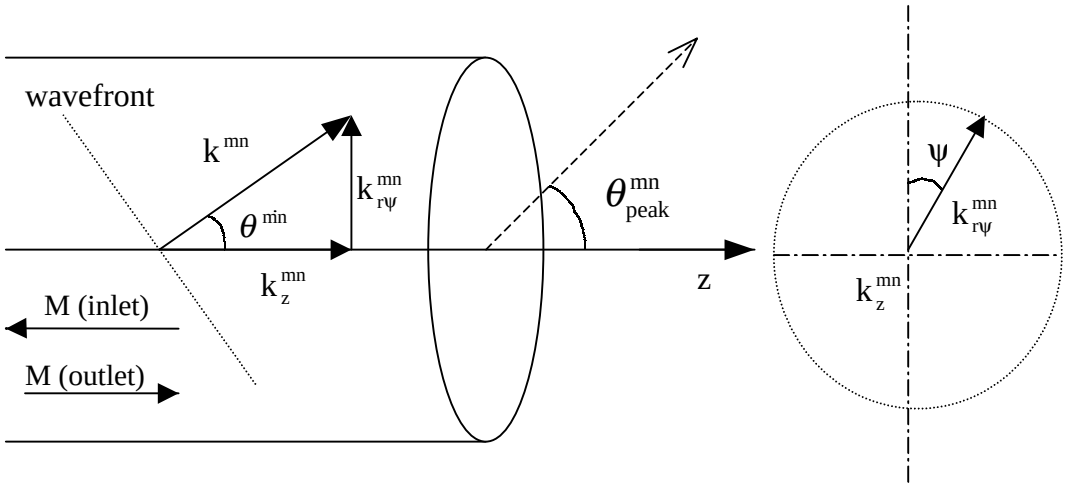

Figure 4.5: Relationship between axial, radial and circumferential wavenumbers.

Noting that the radial wavenumber $k_{r\psi}^{mn}$ denotes the combined radial-circumferential wavenumber in the (r,ψ) plane (Rice and Heidmann 1979), Eq. (4.38) indicates that the wavenumber k^{mn} normal to the wave front of the (m,n) mode is equal to $k - M k_z^{mn}$. The angle θ^{mn} (see Figure 4.5) between the wavefront of the (m,n) mode and the duct axis can therefore be calculated from

$$\cos\theta^{mn} = \frac{k_z^{mn}}{k - M k_z^{mn}}. \tag{4.39}$$

This equation shows that the axial wavenumber k_z^{mn} of a propagating duct acoustic mode is uniquely related to the axial modal propagation angle θ^{mn}. Thus, Eq. (4.39) indicates that for a mode propagating toward the inlet ($-1 \le M \le 0$) or outlet ($0 \le M \le 1$) of the duct, θ^{mn} decreases as k_z^{mn} increases and vice versa.

Furthermore, it has been established (Rice and Heidmann 1979) that the axial modal propagation angle θ^{mn} and the angle of peak radiation θ_{peak}^{mn} are related to the mode cut-off ratio ξ_{mn} (see Eq. (3.7)) as

$$\cos\theta^{mn} = \frac{-M + \sqrt{1 - 1/\xi_{mn}^2}}{1 - M\sqrt{1 - 1/\xi_{mn}^2}} \tag{4.40}$$

and

$$\cos\theta_{peak}^{mn} = \sqrt{1-M^2}\sqrt{\frac{1 - 1/\xi_{mn}^2}{1 - M^2\left(1 - 1/\xi_{mn}^2\right)}}. \tag{4.41}$$

Combining Eqs. (4.39), (4.40) and (4.41) yields the following expression for the angle of peak radiation as a function of the axial wavenumber:

$$\cos\theta_{peak}^{mn} = \left(\frac{2M(1-M^2)k_z^{mn} + (1-M^2)(k_z^{mn\,2}(k - Mk_z^{mn})^{-1} + M^2)}{2M(1-M^2)k_z^{mn} + (1-M^4)(k - Mk_z^{mn})}\right)^{\frac{1}{2}} \tag{4.42}$$

This equation is the basis for the wavenumber sensor control technique; it indicates that the radiated peak far field pressure angle θ_{peak}^{mn} is also uniquely related to the axial wavenumber associated with a given mode. This means that minimizing the modal amplitude of a mode component that propagates with a specific axial wavenumber k_z corresponds to reducing the noise radiated toward a specific direction of the far field (i.e., at the angle of peak radiation of the targeted mode). This relation between the angle of peak radiation and the axial wavenumber of a given mode is presented in Figure 4.6 for five different flow Mach numbers and a free space wavenumber k of 18 m^{-1} (free space wavenumber considered in the active noise control case that is presented in Chapter 6).

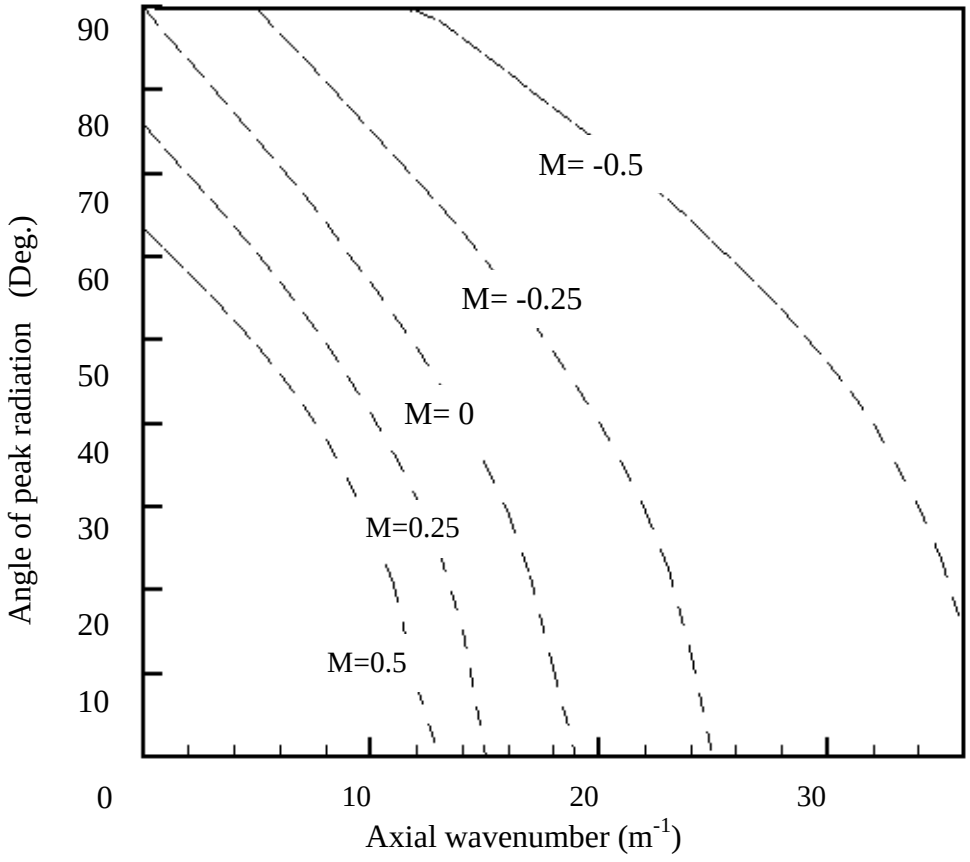

Figure 4.6: Relationship between the axial wavenumber and the angle of peak radiation. k=18.31 m^{-1}.

From this figure, it is seen that for a given free space wavenumber k and flow Mach number M, the angle of peak radiation increases as the axial wavenumber decreases (i.e., as the mode gets closer to cut-off) and vice versa. Therefore, to reduce sound radiation toward the sideline of the duct or towards the ground, the duct modes propagating with the smaller axial wavenumbers have to be targeted for control. Conversely, in order to reduce sound radiation toward the axis of the duct, the modes propagating with the larger axial wavenumbers have to be targeted for control.

The configuration of the control system used for the wavenumber sensor technique is depicted in Figure 4.7.

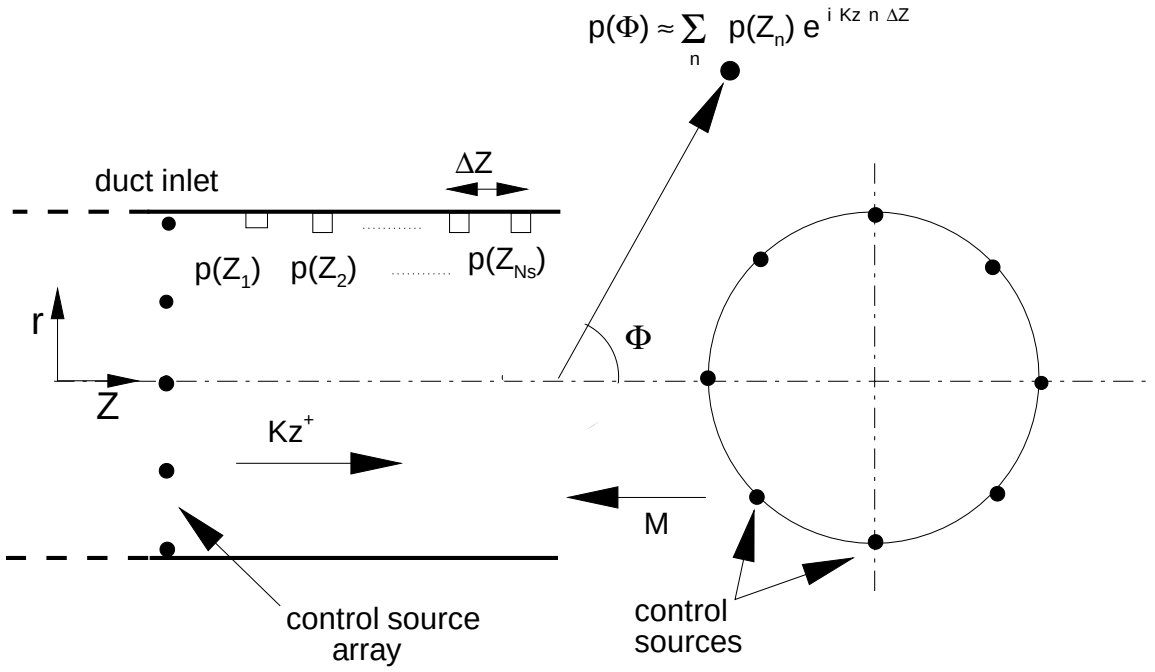

Figure 4.7: Schematic of a control system using inlet wavenumber error sensors.

This control system is designed to detect and target the different modes propagating in the duct based on their axial wavenumbers.

An axial array of N_e pressure sensors is placed along the duct inlet (or outlet) inner wall. The acoustic pressure $p^p_{n_e}$ due to the primary field is computed at the location of these sensors, and these values are used to compute an estimate $T^p(k_z^*)$ of the wavenumber spectrum component corresponding to a target axial wavenumber k_z^*. $T^p(k_z^*)$ is given by

$$T^p(k_z^*) \approx \sum_{n_e=1}^{N_e} p^p_{n_e} \; e^{i\, k_z^*\, n_e\, \Delta z} \tag{4.43.a}$$

which is the wavenumber transform (Fuller et al. 1996)

$$F(k_z) = \int_{-\infty}^{\infty} f(z)\, e^{i\, k_z\, z}\, dz \tag{4.43.b}$$

approximated by a discrete summation over the number of pressure sensors placed along the duct inner wall. Δz corresponds to the spacing between pressure sensors.

The wavenumber spectrum $T^p(k_z)$, $0 \le k_z \le k_z^{\text{Nyquist}}$, gives a decomposition of the in-duct pressure field in terms of the axial wavenumber. It presents peaks at axial wavenumber values that correspond to modes propagating in the duct. The peaks occuring at positive values of k_z correspond to modes propagating toward the duct inlet, while the peaks occuring at negative values of k_z correspond to modes propagating toward the duct outlet. The Nyquist axial wavenumber k_z^{Nyquist} is the highest axial wavenumber that can be resolved by the error sensor array for a particular configuration. It is given by (Hardin 1986)

$$k_{\text{Nyquist}} = \frac{\pi}{\Delta z}. \tag{4.44}$$

Note from Eq. (4.42) that this maximum axial wavenumber also corresponds to a minimum far field angle of peak radiation θ_{peak} that can be resolved by the control system.

In order for the control system to detect properly the wavenumber of the propagating modes, the spacing Δz between pressure sensors must be such that $\Delta z \leq \frac{\lambda_{min}}{2}$, where $\lambda_{min} = \frac{2\pi}{k_{z,max}}$, $k_{z,max}$ being the largest axial wavenumber in the flow. The reason for this criteria is best understood by looking at the example illustrated in Figure 4.8.

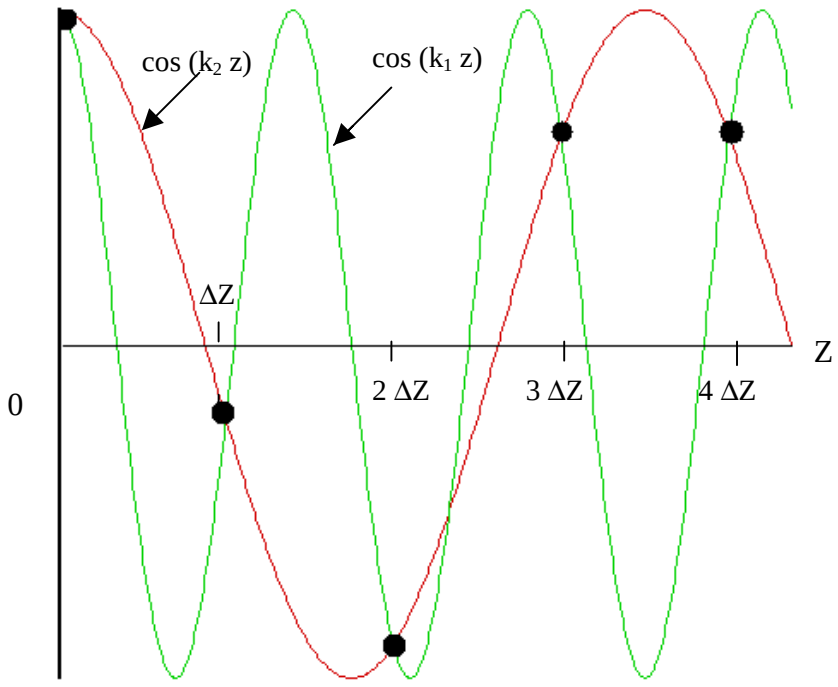

Figure 4.8: Illustration of aliasing.

In that figure, a sinusoidal signal cos (k_1 z) of wavelength $\lambda_1 = \frac{2\pi}{k_1}$ is sampled at a rate $\Delta z \geq \frac{\lambda_1}{2}$ (the dots represent samples). From the sampled data, the sinusoid cos (k_2 z) of wavelength $\lambda_2 = \frac{2\pi}{k_2}$ is seen to be indistinguishable from the sinusoid of wavelength λ_1. The signal cos (k_1 z) can not be recognized from the sample data and is instead identified as being the signal cos (k_2 z). This phenomenon is called aliasing, and is the reason why a sampling rate (i.e., Δz) of no more than half the minimum wavelength must be used where data having a minimum wavelength are analyzed.

A single array of control sources is used to generate the control field that will minimize $T^p(k_z^*)$. In order to ensure the generation of the desired control spinning modes, the control source array is configured as described in section 4.2.2 for the fuselage error sensor technique. An estimate $T^s(k_z^*)$ (due to the secondary field) of the wavenumber spectrum component corresponding to the target axial wavenumber k_z^* is given by

$$T^s(k_z^*) \approx \sum_{n_e=1}^{N_e} p_{n_e}^s \; e^{i\, k_z^* n_e\, \Delta z}. \tag{4.45}$$

$p_{n_e}^s$ is the pressure at the n_e^{th} error sensor due to all the control sources. It is defined as

$$p_{n_e}^s = U_0\,(R)\,(p_{n_e,s})_{s=1,2,\ldots,S} \tag{4.46}$$

where U_0 is the control input driving each control source, (R) is the configuration vector for the control source array (defined as in section 4.2.2), and $(p_{n_e,s})_{s=1,\ldots,S}$ is a vector whose elements $p_{n_e,s}$ correspond to the pressure at the n_e^{th} pressure sensor due to the s^{th} control source.

The optimum control input $(U_0)_{opt}$ is determined such that

$$T^{p}(k_z^*) + T^{s}(k_z^*) = 0. \tag{4.47}$$

Therefore,

$$(U_0)_{opt} = -\frac{T^{p}(k_z^*)}{\sum_{n_e=1}^{N_e} (R)(p_{n_e,s})_{s=1,2,...,S}\, e^{i k_z^* n_e \Delta z}}. \tag{4.48}$$

Thus, by minimizing a specific wavenumber component of the spectrum at one particular frequency, the control system targets the mode that propagates in the duct with that specific axial wavenumber and achieves noise reduction at the angle of peak radiation of the targeted mode. Hence, targeting the lower wavenumber components will attenuate the radiation toward the sideline of the duct, while minimizing the higher wavenumbers will reduce the noise radiated more the duct axis.